Path length control in a nulling coronagraph with a MEMS deformable mirror and a calibration interferometer.

Shanti R. Rao*[a], J. Kent Wallace[a], Rocco Samuele[b], Supriya Chakrabarti[c],
Timothy Cook[c], Brian Hicks[c], Paul Jung[c], Benjamin Lane[d], B. Martin Levine[a],
Chris Mendillo[c], Edouard Schmidtlin, Mike Shao[a], Jason B. Stewart[c]

[a]Jet Propulsion Laboratory, California Institute of Technology,
4800 Oak Grove Dr, Pasadena, CA, USA 91101;
[b]Northrop Grumman Space Technologies, 1 Space Park Blvd., Redondo Beach, CA USA 90278;
[c]Boston University Center for Space Physics, 725 Commonwealth Blvd, Boston MA 02215;
[d]Draper Laboratory, 555 Technology Square, Cambridge, MA 02139

ABSTRACT

We report progress on a nulling coronagraph intended for direct imaging of extrasolar planets. White light is suppressed in an interferometer, and phase errors are measured by a second interferometer. A 1020-pixel MEMS deformable mirror in the first interferometer adjusts the path length across the pupil. A feedback control system reduces deflections of the deformable mirror to order of 1 nm rms.

Keywords: Nulling coronagraph, extrasolar planet, calibration interferometer, MEMS adaptive optics, deformable mirror

1. INTRODUCTION

A nulling coronagraph [1,2] is an instrument intended for observing planets orbiting nearby stars. Placed at a pupil relay of a telescope, it uses destructive interference to suppress a white light point source. Properly aligned, the target star is at a dark fringe (the "null") and its planets at a bright fringe. Since stars are 10^7 to 10^{10} times [3] brighter than their planets, this instrument is sensitive to optical phase aberration, which we compensate with a MEMS deformable mirror (DM).

Our implementation of a nulling coronagraph is a Mach-Zender interferometer, where one arm has a 1020-element DM from Boston Micromachines Corporation, and the other arm has a gold-coated flat mirror mounted on a PZT tip/tilt/piston stage. With the addition of dispersion elements, the coronagraph would be a Visible Nulling Coronagraph [4,5] similar to that proposed for the Terrestrial Planet Finder. See Guyon et al [6] for a discussion of the relative merits of several coronagraph schemes proposed for imaging extrasolar planets.

Previous experiments with nulling interferometers, or "nullers", have achieved suppression ratios of 10^6 in laser and in 20% bandpass white light [7,8], as measured by a fiber-coupled outputs. These experiments demonstrated control of path length stability, dispersion, and polarization, though not of intensity. In this new coronagraph, the output forms an image on a CCD camera. The input light source is a single-mode fiber, so the image is a direct measurement of the interferometer's point-spread function (PSF).

We also demonstrate the use of a calibration interferometer, based on the scheme proposed by Wallace et. al. [11,12]. The calibration interferometer mixes the dark port of the nuller (corresponding to planet light plus suppressed starlight, or in this case the residual speckle pattern of the nuller) with spatially filtered star light from the bright port. This technique is applicable to instruments like the Gemini Planet Imager [9] and NASA's PICTURE sounding rocket (Planet Imaging Coronagraph Telescope Using a Rocket Experiement) [10]. The optical layout here is nearly identical to that in PICTURE, and the algorithm we describe could be slightly modified to work with the Gemini Planet Imager.

The calibration interferometer allows us to correct path errors in the nuller, without large changes to the nuller's path length, as in traditional phase-shifting interferometry. For astronomers, this means that the coronagraph can calibrate itself while observing a star, minimizing wasted telescope time.

*shanti.r.rao@jpl.nasa.gov; phone 1-818-393-7246

2. METHODS

2.1 Experiment setup

The schematic of the optical layout is shown in Fig. 1. The light source (0) is either a 632nm diode laser or a 3100K tungsten-halogen lamp, coupled to a single-mode fiber. The output of this fiber is collimated by an off-axis parabolic mirror (1) and enters the nuller at the first beamsplitter (2). The output of the nuller is at the second beamsplitter (3), with its reflecting surface parallel to the first beamsplitter, but with the opposite orientation so that each arm of the coronagraph passes through an equal amount of glass.

A MEMS deformable mirror (5 DM) from Boston Micromachines Corporation (BMC)[14] is in one arm of the nulling coronagraph. This DM has 1020 active actuators on a continuous face sheet, with a stroke range of 1.6 microns. The actuators are 340 microns square, on a 32x32 grid. Four actuators near the edge are not active, to make room for ground pins. We have used this apparatus with several MEMS DMs from BMC with success by excluding from feedback control actuators close to surface defects.

Opposite the DM is a mirror (6 TTP) on a 3-axis tip/tilt/piston stage. The DM and the TTP mirror were coated with gold at the same time, so as to match reflectivity.
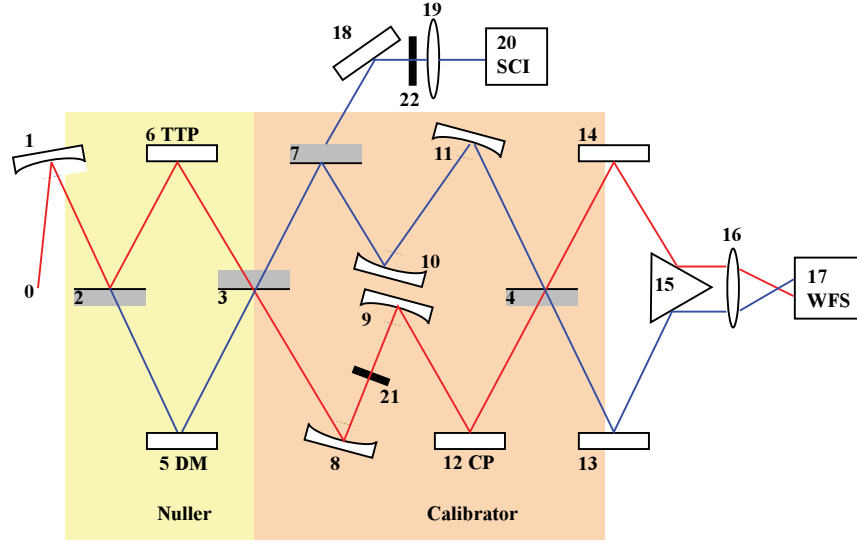

Fig. 1. Optical layout of the nuller and calibrator. The red line follows the symmetric ports, the blue line the asymmetric.

The dark port of the nuller goes through a beamsplitter (7) and is steered (18) through a Lyot stop (22) and focused (19) onto a "Science camera" (20 SCI). If this instrument were looking at a star, this detector would see an image of the planets, plus the residual speckle pattern from the starlight. Some of the light from the dark port is reflected off the beamsplitter (7) and is used in the calibrator.

The calibrator's input beamsplitter is the same optic as the nuller's output beamsplitter (3). The nuller's dark port forms the calibrator's "measurement" arm, while the nuller's bright port forms the calibrator's "reference" arm. In the measurement arm, the pupil is inverted through a focus by mirrors (10, 11). In the reference arm, the light passes through a similar mirror system (8, 9), and through a pinhole (21) a few microns in diameter. The effect of the pinhole is to remove spatial detail from the reference arm, so that it contains only the low-order modes of light rejected by the nuller.

The reference and measurement beams are recombined at a final beamsplitter (4), again oriented opposite to the input beamsplitter (3). Fold mirrors (13, 14, 15) direct both calibrator outputs to the wavefront sensor camera (17 WFS), with a lens (16) adjusted so that the WFS images the pupil at the DM (5).

In the calibrator, the pinhole input mirror (8), mounted on a 3-axis PZT stage, can be rotated to use the pinhole (21) as a shutter to allow us to adjust the DM and TTP mirrors in the nuller before activating the calibrator. The "calibrator piston" mirror (12 CP) in the reference arm moves along 1 axis to change the phase for the calibration algorithm.

2.2 Electronics

Control voltages for the DM are generated by a bank of 14-bit D/A converters [13]. The other active elements, the TTP, CP and Pinhole mirrors, are mounted on PZT stages. A computer reads out the WFS and SCI cameras and generates control signals for the effectors (Fig. 2).
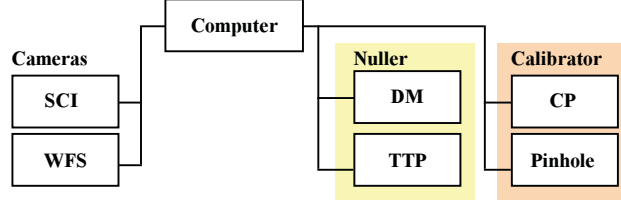

Fig. 2. System block diagram. The wavefront sensor camera (WFS) is the primary input into the control loop. The DM, TTP, and CP mirrors are the feedback effectors. The Pinhole mirror is only moved when switching between modes.

2.3 Startup

The first step is to select an operating point for the nuller. With the pinhole blocked, the WFS shows the interference pattern at the DM, as seen through the nuller's dark port. We move the TTP mirror through the center of its range and, with white light illuminating the nuller, identify the central fringe. A second scan, with steps of a few nanometers, shows the central fringes in more detail. We select the darkest point as our initial position for the TTP mirror, and calculate the distance between bright and dark fringes. (Fig. 3).
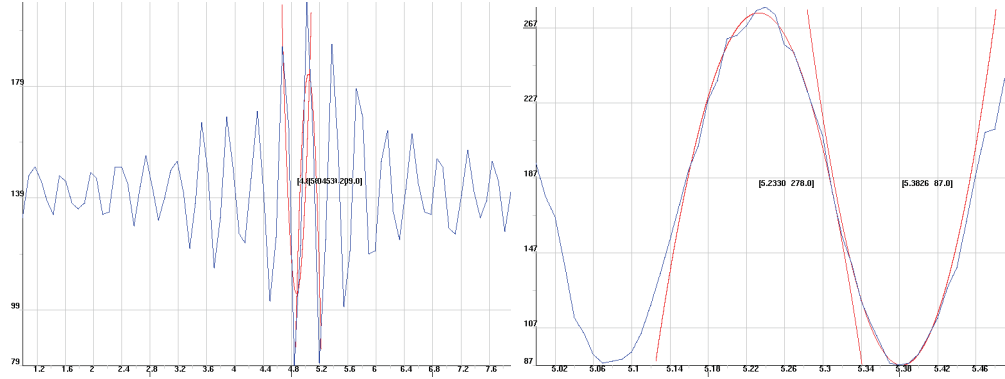

Fig. 3. Scanning the fringe with the TTP actuator. Left: the TTP moves over a large range to find the white light fringe. Right: zooming in on the central fringe. The horizontal axes are displacements, in approximate microns, and the vertical axes are intensity measured by the WFS on a single pixel (arbitrary units). The red lines are parabolic fits to the maxima and minima of each fringe scan.

The TTP mirror then stepped through 0°, 90°, 180°, and 270° steps to capture *A*, *B*, *C*, and *D* images, respectively, of the nuller pupil. The phase error across the nuller pupil is calculated as $\tan^{-1}((D\text{-}B)/(C\text{-}A))$, and the 2-dimensional phase map is unwrapped and used to rotate the TTP mirror about its center to remove tilt fringes. The order of subtraction *D-B*, *C-A* is chosen so that 0° measured at the dark port corresponds to maximum transmission at the bright port of the nuller.

To register the WFS with respect to the DM, we take two phase maps before and after applying a low voltage to four actuators equally distributed about the center of the DM. This lets us account for rotation of the camera with respect to the DM's actuator grid, and measure differences in scale between the DM actuators and WFS pixels. (Each DM actuator corresponds to a 5 x 5 grid of pixels on the WFS, rotated by a few degrees.) The rotation and scale are used when using the WFS data to update the DM actuator positions.

2.4 Nulling

Still looking only at the nuller's interference pattern, we seek to flatten the wavefront across the deformable mirror by iterating the following procedure, illustrated in Fig. 4:

1. Phase-step the TTP mirror in 90° steps, and capture simultaneous images from the WFS camera.

2. From the 4 phase-stepping images, compute the unwrapped phase across the pupil, then downsample the phase onto the DM coordinate system.

3. Tip, tilt, and piston are subtracted from the error signal and applied to the TTP mirror. Meanwhile, each DM actuator is controlled with a simple integrator servo. Using the phase map from step 2 as the error signal, update each actuator's setpoint. The voltage applied to the DM actuator is proportional to the square root of the setpoint.

After the 6th iteration, the actuator displacement error over the central region of the DM is 40nm rms, and incremental updates move the actuators by an average of 4nm per step.
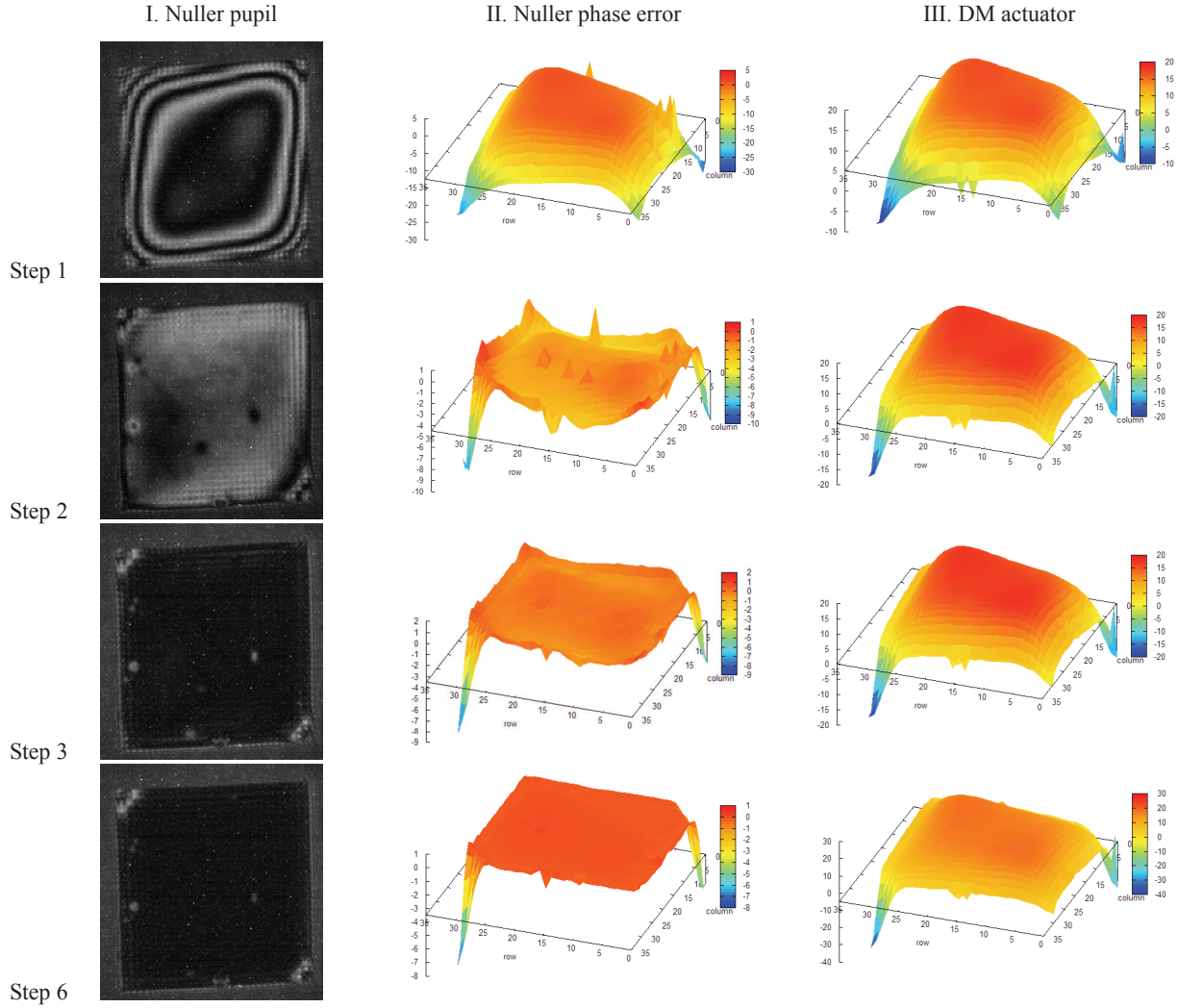

Fig. 4. Flattening the nuller with a white light source in 6 steps. Columns are: I. Nuller pupil image at 0°; II. The nuller phase error map (in the DM coordinate system, Z-axis in radians); III. The state of the setpoints for the DM (in the DM coordinate system, Z-axis in radians). This particular DM has a few defects and strong curvature at two corners, which are ignored by the control system. Steps 4 and 5 are omitted for clarity. A movie of this can be found online.

Video 1. Ten sequential nuller pupil images at 0°, as in Fig. 4. http://dx.doi.org/

2.5 Calibrating

Once the nulling algorithm has reached a steady state, the Pinhole mirror is rotated back into position, and the calibration interferometer's fringe pattern appears on the WFS. Though the feedback and actuation mechanism is the same as before, calculating the error signal is a little more involved. At the outputs of the nuller, the fields at the dark (E_D,

asymmetric) and bright (E_B, symmetric) ports differ in phase by 180º. If we let E_0 be the electric field incident on the nuller, and assuming perfect 50% beamsplitters, we can write these output fields as

$$E_D = \frac{1}{2}E_0 e^{i(\theta_{DM})}e^{i\omega t} + \frac{1}{2}E_0 e^{i(\theta_{TTP}+\pi)}e^{i\omega t}$$

$$E_B = \frac{1}{2}E_0 e^{i(\theta_{DM}+\pi)}e^{i\omega t} + \frac{1}{2}E_0 e^{i(\theta_{TTP}+\pi)}e^{i\omega t}$$

The difference between them is a π phase shift at the nuller's output mirror (3). The corresponding intensities I_D and I_B at the nuller outputs are

$$I_D = E_0^2[1 - \cos(\theta_{DM} - \theta_{TTP})]$$

$$I_B = E_0^2[1 + \cos(\theta_{DM} - \theta_{TTP})]$$

The calibrator combines the electric fields E_D (attenuated by factor d at the beamsplitter (7)) and E_B (attenuated by factor b at the pinhole (21)), and adds a phase shift ϕ to the bright arm. Its asymmetric E_A and symmetric E_S output fields are

$$E_A = dE_D + bE_B e^{i\phi}$$

$$E_S = dE_D e^{i\pi} + bE_B e^{i\phi}$$

Remembering that we are operating near the point where $\theta_{DM} = \theta_{TTP}$, it is convenient to write the corresponding intensities I_A and I_S seen by the WFS camera (17) as

$$I_A = d^2|E_D|^2 + b^2|E_B|^2 + dbE_0^2 \sin(\theta_{DM} - \theta_{TTP})\sin(\phi)$$

$$I_S = d^2|E_D|^2 + b^2|E_B|^2 - dbE_0^2 \sin(\theta_{DM} - \theta_{TTP})\sin(\phi)$$

If we vary the calibrator phase shift ϕ by 360º without moving the DM or TTP, the change in intensity measured at the WFS will be proportional to the phase error in the nuller, $\theta_{DM} - \theta_{TTP}$. We can choose to minimize the variable $aE_0^2 \sin(\theta_{DM} - \theta_{TTP})$, the visibility of the calibration interferometer. To measure visibility, we capture WFS images with the CP at ϕ = 0°, 90°, 180°, and 270° (*A*, *B*, *C*, and *D*, respectively) while dithering the path length in the nuller by 15nm.

To minimize the nuller path length, the TTP mirror is moves to positions of -15nm, 0nm, and +15nm prior to acquiring each set of *ABCD* images. From the resulting set of 12 images, we calculate three visibility images (Fig. 5).

Since the WFS sees both outputs of the calibration interferometer, you could measure the 0° and 180° images at the same time — one image from each side of the beamsplitter (4) — and similarly for 90° and 270°. For this experiment, we stepped the CP mirror through five positions (the last being 360°) so that we could verify that the step sizes were accurate to ±2 nm. You would want to use this shortcut if you were looking at an actual star.

Note that we are not minimizing the amplitude of the field at the WFS, but the visibility. In fact, the phase of the field, proportional to (*B* - *D*) / (*A* + *B* + *C* + *D*), is all we need. The more time-consuming process we use here is robust to errors in ϕ, in that the CP stepping sequence doesn't need to start at a well-defined position, so long as the sizes of the phase steps are correct. Additionally, since (*A* - *C*) / (*A* + *B* + *C* + *D*) measures the field amplitude, *ABCD* provides enough information to reconstruct the PSF at the science camera pupil, useful for noise reduction post-processing.
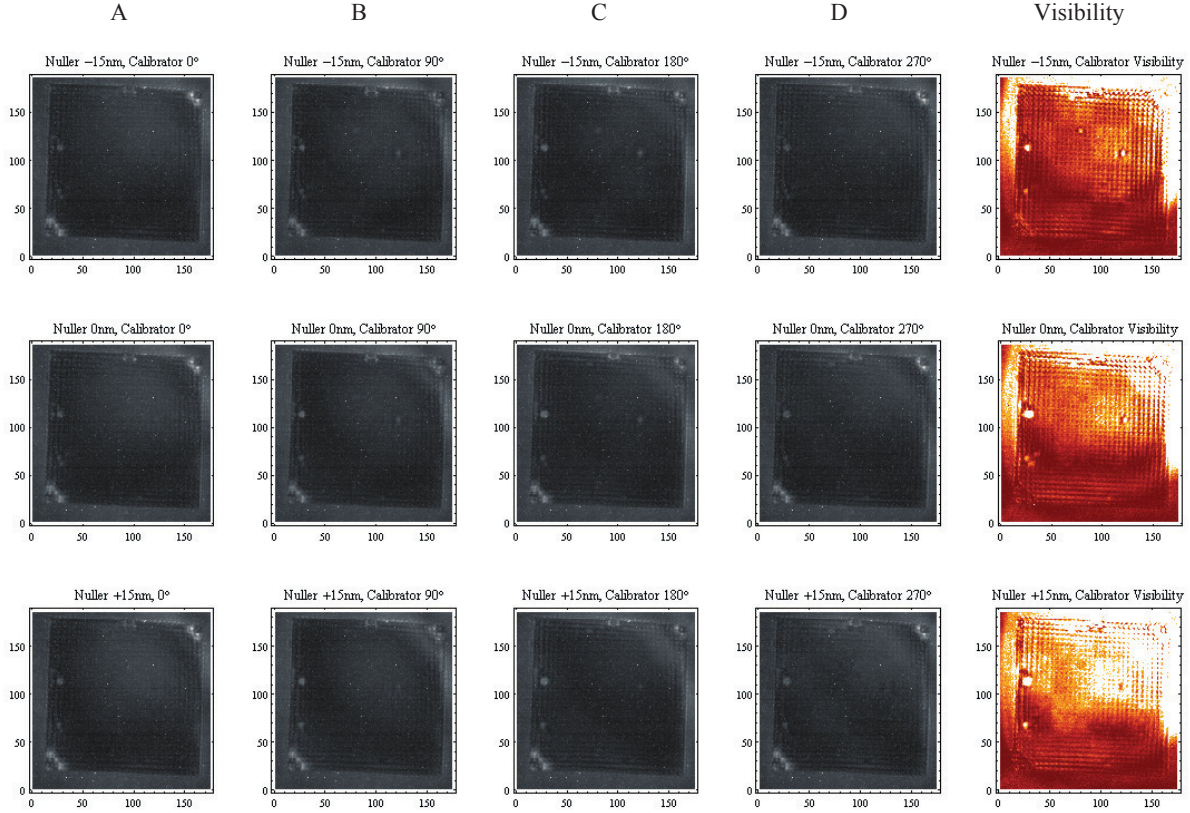
Fig. 5. One set of measurements for the calibration algorithm on white light. A 4x4 checkerboard, 5nm high, has been introduced onto the DM and is apparent in the calibrator visibility if not on the interference pattern. The nuller TTP mirror is moved in and out by 15nm, while pupil images are captured at 90° phase steps in the calibrator. Visibility is calculated as $(A\text{-}C)^2 + (B\text{-}D)^2$. Note: The Y axis is inverted with respect to Fig. 4.

Then, for each DM actuator, we fit a parabola to the 3 visibility measurements, and compute the displacement that will minimize the visibility. This displacement map is the error signal for the deformable mirror, and we do step #3 from the nulling servo. Calculation of the error signal is susceptible to camera noise, so we run a statistical test on the error signal map and do not move those DM actuators which appear to be outliers.

As this process repeats, the step size decreases from 15nm to 7nm as the error variance shrinks. For demonstration, we added a disturbance of 0 to 5nm to the flattened DM, and then activated the calibrator servo. Fig. 5 shows the first step, and Fig. 6 shows the calibrator error signal after the 29th iteration of the algorithm (still using a white light source), when the variance in actuator displacements is 2nm rms and the checkerboard pattern is no longer distinguishable.

Fluctuations on the order of 1nm could be caused by mechanical vibration in the optic mounts or noise in the TTP actuators. We are working on improving these.
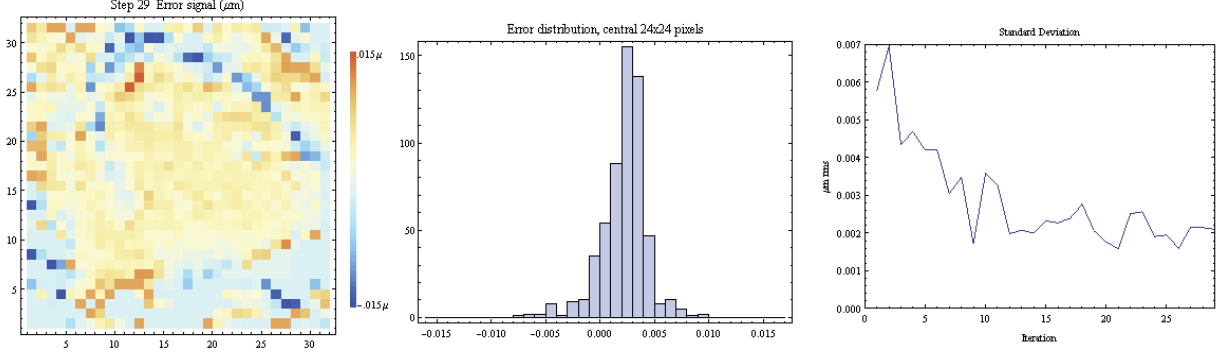
Fig. 6. Left: Error signal for the deformable mirror after 29 iterations of the calibration algorithm with white light. Middle: Histogram of the distribution of error signal for the central DM actuators. The X axis is microns, Y axis the number of DM actuators. Right: The variance of the error signal as a function iteration number. The DM's curvature is too steep to measure for 3 actuators at the top left and bottom right corners, so these are set to 0 in software.

3. RESULTS

We use a brighter laser source to look at the images formed by the calibrated interferometer. Fig. 7 shows the output of the nuller at constructive interference (left, nuller phase = 180°) and destructive interference (right, nuller phase = 0°).
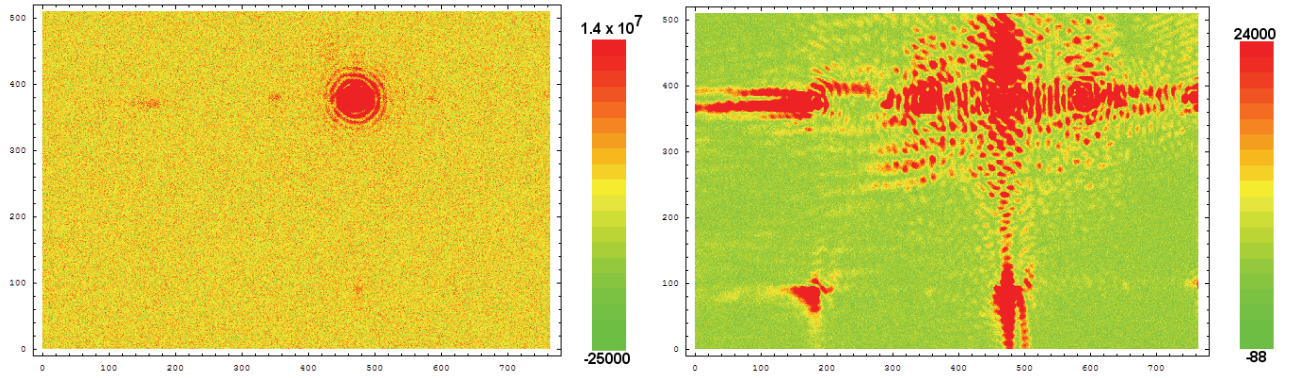

Fig. 7. Images of a single-mode fiber tip at the SCI camera. Left: PSF at maximum constructive interference. Right: PSF at maximum destructive interference. The images are taken at different exposure times, and the pixel values offset and scaled so that they are proportional to the relative number of photons that would be detected if the exposure times were the same. The perpendicular diffraction features are probably caused by surface roughness on DM. The light source for these images is laser at 633nm.

Taking a picture of an extrasolar planet is a matter of not looking directly at the star. This particular instrument is tuned to observe the putative planet around Epsilon Eridani [15,16] when the planet is slightly farther away from us than is the star. Based on a recent estimate of the planetary parameters from radial velocity measurements [17], we expect that the planet image will be somewhere on the first minimum of the star's Airy disk.

At the darkest points of the nulled speckle pattern on the 1st Airy ring , the nulled PSF for laser light is 10^{-4} as bright as at the center of the Airy disk. If one were to slowly rotate the telescope about the star, a planet 10,000 dimmer than its host star would be noticeable. If not for the coronagraph, the Airy rings would be about 10^{-2} times as bright as at the center, obliterating any hope of imaging a planet.

The suppression ratio within the central Airy spot is 600:1 in laser light, whereas an interferometer with 1.5nm path length error would be expected to be limited to 4500:1. The other dominant error sources — pupil rotation, birefringence, reflectivity mismatch, and dispersion [18] — set higher limits. A possible explanation is the "scalloping" effect we see on our DM, the sub-actuator structure visible in the interferograms in Fig. 4.

A cross-section of the unwrapped phase of the corrected DM (Fig. 8) reveals systematic bumps on the DM surface, at too high a spatial frequency to be corrected by the DM itself. At our WFS resolution of five times the actuator pitch, the surface displacement variation is on the order of 15 nm rms at the center of the DM, increasing to hundreds of nm towards the corners. The corners show the strongest effect, and are masked before the SCI camera.
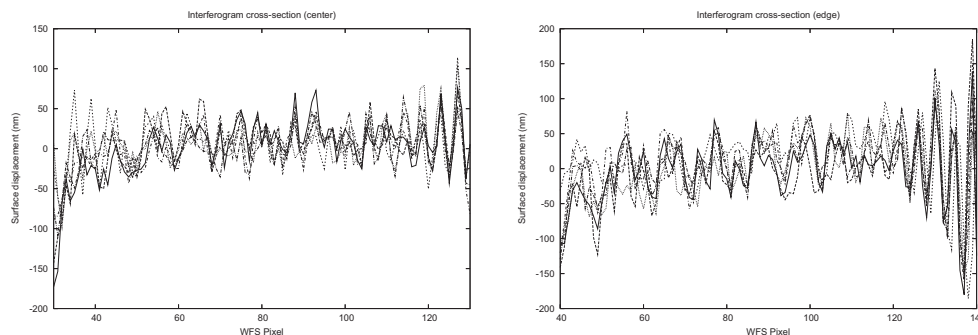

Fig. 8. Several adjacent, horizontal cross-sections of the interferogram of the flattened DM, through the center and near the edge. Five pixels equal one actuator.

After path length error, the next largest limitation would be reflectivity mismatch between the arms of the nuller. The TTP mirror has a zerodur substrate, whereas the DM is made of silicon, but both were coated with gold at the same time, in the same coating chamber, and we have measured their reflectivity mismatch to be on the order of 0.01, which would limit the suppression ratio to 4×10^4, much larger than what we observe.

4. CONCLUSIONS

This work demonstrates a deformable mirror for path length control in an interferometer, and the utility provided by a calibration interferometer. The calibrator allows us to quickly reduce the nuller's path length errors from 40nm rms to 2nm rms in a few seconds, free of the large changes in the nuller's output intensity that accompany traditional phase-stepping algorithms.

The success of the calibration interferometer shows in the image plane, where there are enduring dark holes near the center of the PSF, at positions suitable for imaging extrasolar planets, despite the overall brightness of the speckle pattern. The MEMS deformable mirrors we used are prototypes, and advances in fabrication will improve this instrument's capability.

ACKNOWLEDGEMENTS

REFERENCES

[1] J. Gay, Y. Rabbia, "Principe d'un coronographe interferential" C. R. Acad. Sci. Paris 322, Ser. II b, **265** (1996).
[2] P. Baudoz, Y. Rabbia, J. Gay "Achromatic interfero coronagraphy", Astron. Astrophys. Suppl. Ser. **141**, 319-329 (2000).

[3] A. Burrows, "A Theoretical Look at the Direct Detection of Giant Planets Outside the Solar System," Nature, Vol **433**, January 20, 2005

[4] B. M. Levine, M. Shao, D. T. Liu, J. K. Wallace, B. Lane, "Planet detection in visible light with a single aperture telescope and nulling coronagraph", Proc. SPIE **5170**, 200-208 (2003)

[5] R. G. Lyon et. al., "Visible Nulling Coronagraphy for Exo-Planetary Detection and Characterization", Proc. IAU **200**, 345-352 (2006)

[6] O. Guyon, E. A. Pluzhnik, M. J. Kuchner, B. Collins, and S. T. Ridgway, "Theoretical limits on extrasolar terrestrial planet detection with coronagraphs." The Astrophysical Journal Supplement Series **167**, 81-99, (2006).

[7] E. Schmidtlin, J. K. Wallace, R Samuele, B. M. Levine, and M. Shao, "Recent progress of visible light nulling interferometry and first 1 million null result", *Direction Imaging of Exolplanets: Science and Techniques,* IAU Colloquium **200** (2005).

[8] R. Samuele, J. K. Wallace, E Schmidtlin, B. M. Levine, M. Shao, "Experimental Progress and Results of a Visible Nulling Coronagraph", *Proceedings of the IEEE Aerospace conference* (2007).

[9] B. Mackintosh et al., "The Gemini Planet Imager", *Advances in Adaptive Optics II,* Proc. SPIE, **6272** (2006)

[10] M. Shao, J. J. Green, B. Lane, J. K. Wallace, B. M. Levine, R. Samuele, S. R. Rao and E. Schmidtlin, "Calibration of Residual Speckle Pattern in a Coronagraph", Proceedings of the International Astronomical Union **1,** 525-528 (2005).

[11] J. K. Wallace, J. J. Green, M. Shao, T. Mitchel, J Lloyd, B MacIntosh, "Science camera calibration for extreme adaptive optics", Astronomical Telescopes and Instrumentation (2004) http://hdl.handle.net/2014/38945

[12] B. F. Lane, M. W. Muterspaugh, M. Shao, "Calibrating on an Interferometric Null", ApJ **648**, 1276-1284 (2006)

[13] S. Rao, "Driver code for adaptive optics", NASA Tech Briefs (2007) http://techbriefs.com/content/view/1187/34/

[14] Boston Micromachines Corporation, http://bostonmicromachines.com/

[15] B. Campbell, G. A. H. Walker, and S. Yang, "A Search for Substellar Companions to Solar-Type Stars", ApJ. **331**, 902-921 (**1988**). doi:10.1086/166608

[16] A. Cumming, G. Marcy, and R. P. Butler, "The Lick Planet Search: Detectability and Mass Thresholds", ApJ. **526**, 890-915 (1999). doi:10.1086/308020

[17] A. P. Hatzes et. al., "Evidence for a Long-Period Planet Orbiting Epsilon Eridani", ApJ. **544**, 145-148 (2000) doi:10.1086/317319

[18] E. Serabyn, "Nulling interferometry: symmetry requirements and experimental results", Proc. SPIE, **4006**, 328 (2000). doi:10.1117/12.390223